Journal of Vacuum Science and Technology A

RESEARCH ARTICLE | JANUARY 04 2024

Near-surface electronic structure An x-ray absorption spectroscopy s

Special Collection: Special Collection Commemorating the Career of Frederick J

S. Sahra. K; Autgp; Fa Rd; C. Lu; C. Kr; Dis A. Aena

J. aV. Sc hno 42, A012702 (2024)
https://doi.org/10.1300.915

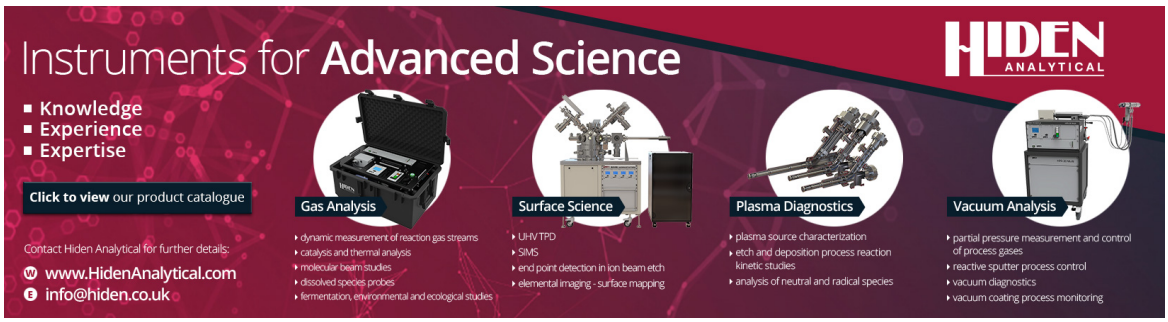

JVST A
Journal of Vacuum Science & Technology A

ARTICLE

pubs.aip.org/avs/jva

Near-surface electronic structure in strained Ni-ferrite films: An x-ray absorption spectroscopy study

Cite as: J. Vac. Sci. Technol. A 42, 012702 (2024); doi: 10.1116/6.0003095
Submitted: 28 August 2023 · Accepted: 1 December 2023 ·
Published Online: 4 January 2024

S. Saha,[1] R. Knut,[2] A. Gupta,[3] F. Radu,[4] C. Luo,[4,5] O. Karis,[2] and D. A. Arena[6,a)]

AFFILIATIONS

[1]Department of Physics, Ashoka University, Sonipat, Haryana 131029, India
[2]Department of Physics and Astronomy, Uppsala University, SE-75120 Uppsala, Sweden
[3]Department of Chemistry and Biochemistry, The University of Alabama, Tuscaloosa, Alabama 35487
[4]Helmholtz-Zentrum Berlin für Materialien und Energie, Albert-Einstein-Strasse 15, 12489 Berlin, Germany
[5]Institute of Experimental Physics of Functional Spin Systems, Technical University of Munich, James-Franck-Strasse 1, 85748 Garching b. München, Germany
[6]Department of Physics, University of South Florida, Tampa, Florida 33620

Note: This paper is part of the Special Topic Collection Commemorating the Career of Frederick J. Walker.
[a)]**Author to whom correspondence should be addressed:** darena@usf.edu

ABSTRACT

We report on the x-ray absorption spectra (XAS) and x-ray magnetic circular dichroism (XMCD) of a series of $NiFe_2O_4$ (Ni ferrite) films grown on symmetry matched substrates and measured in two geometries: out-of-plane and near in-plane. The Ni ferrite films, grown by pulsed laser deposition, are epitaxial and the substrates used ($ZnGa_2O_4$, $CoGa_2O_4$, $MgGa_2O_4$, and $MgAl_2O_4$) introduce a systematic variation in the lattice mismatch between the substrate and the film. Modeling of the XAS and XMCD spectra, both measured with the surface sensitive total electron yield mode, indicates that the Ni^{2+} cations reside on the octahedrally coordinated lattice sites in the spinel structure. Analyses of the Fe XAS and XMCD spectra are consistent with Fe^{3+} cations occupying a subset of the octahedral and tetrahedral sites in the spinel oxide lattice with the addition of a small amount of Fe^{2+} located on octahedral sites. The Ni^{2+} orbital to spin moment ratio (μ_ℓ/μ_s), derived from the application of XMCD sum rules, is enhanced for the substrates with a small lattice mismatch relative to $NiFe_2O_4$. The results suggest a path for increasing the orbital moment in $NiFe_2O_4$ by applying thin film growth techniques that can maintain a highly strained lattice for the $NiFe_2O_4$ film.

I. INTRODUCTION

Magnetically ordered insulators with anti-ferromagnetic interactions are of crucial importance to diverse applications including power electronics,[1] active and passive microwave and mm-wave components,[2] spintronic devices,[3,4] and they are also the parent compounds of many classes of high-temperature superconductors.[5] The incorporation of magnetic insulators[6,7] into integrated electronics generally requires either polycrystalline or epitaxial thin films. In the case of epitaxial films, strain imparted by the substrate can have profound effects on the properties of the film.[8–17]

Extremely high strain states have been generated in epitaxial oxide thin films; for perovskite ultrathin films grown on symmetry-matched perovskite substrates, strain states as high as 6% have been realized.[18] Moreover, epitaxial strain in oxide thin films has been exploited to produce higher temperature superconductors;[9] stabilize ferromagnetism;[19,20] activate piezo- and ferroelectricity;[18] modify dielectric constants and optical bandgaps;[21] and drastically alter catalytic activity.[22] As many magnetic insulators based on the spinel structure can also be grown in thin film forms, a natural issue to explore is the role of epitaxial strain on the properties of

such spinel oxide thin films. Among the broad group of magnetic insulators,[6] spinel ferrites[23–25] are commonly used for applications requiring high-resistivity, low loss performance at high frequencies, and high magnetic permeability. Ni ferrite ($NiFe_2O_4$)[3,26] is a magnetically soft spinel compound that in the bulk exhibits a Curie temperature over 850 K,[27] high electrical resistivity,[28] large bandgap,[29] and retains a significant magnetization of ∼ 50 emu/g, or about 2.1 μ_B per formula unit.[30–32] In thin film form and when grown on well-lattice matched substrates, $NiFe_2O_4$ is an intriguing spintronic material with very low Gilbert damping,[33] making it attractive for applications that rely on spin transport and magnon propagation.[34,35] Also, $NiFe_2O_4$ is a low cost material with useful catalytic properties.[36,37] Spin transport across interfaces relies on the electronic structure near the surface of the growing $NiFe_2O_4$ film, and similarly catalytic reactions are mediated by the electronic states on the surface. As the electronic structure of materials can be modified significantly by strain,[38,39] it is of considerable importance to explore the electronic states of strained $NiFe_2O_4$ films in the near-surface region.

Spinel oxide compounds have the general formula AB_2O_4. The A cations are divalent while the B cations are trivalent; in *spinel ferrites* the *B* cations are Fe^{3+}. Spinel oxides have a relatively open cubic crystal structure where the O^{2-} anions form a fcc lattice, leading to a network of tetrahedrally (T_D) and octahedrally (O_H) coordinated sites for the cations. The cations in the spinel structure are distributed among one half of the available O_H sites and one eighth of the T_D sites. Magnetically, the dominant exchange interaction in spinel compounds is the anti-ferromagnetic exchange between the T_D and the O_H sub-lattices, while the T_D–T_D and O_H–O_H interactions are ferromagnetic. $NiFe_2O_4$ (or NFO) is an *inverse spinel*, where the Fe^{3+} cations are divided equally between the O_H and T_D sites, leading to near-complete cancelation of the ∼5 μ_B moment per Fe^{3+} cations, while the divalent Ni cations with a moment of ∼ 2 μ_B reside on the remaining O_H sublattice sites and provide most of the net moment in NFO.

In this article, we report on an x-ray spectroscopic study of NFO films grown on different spinel oxide substrates: $ZnGa_2O_4$ (ZGO), $CoFe_2O_4$ (CFO), $MgGa_2O_4$ (MGO), and $MgAl_2O_4$ (MAO). The selection of different spinel oxide substrates is significant for two main reasons. First, in contrast to films grown on substrates with rocksalt or perovskite lattices, such as MgO or $SrTiO_3$, the similar crystal symmetry between the spinel substrate and NFO film helps reduce defects such as formation of anti-phase boundaries. Second, the four different spinel substrates permit tuning of the lattice mistmatch between the film and substrate.

The bulk cubic lattice constant of NFO (a_{bulk}^{NFO}) has been reported as 8.345 Å[33] and 8.337 Å,[40] and hence we will refer to the average value of 8.341 Å. ZGO ($a^{ZGO} = 8.333$ Å[40]) is almost perfectly matched with NFO, leading to a lattice mismatch of only 0.10%. At the other extreme, MAO ($a^{MAO} = 8.086$ Å[33]) has a smaller lattice parameter, leading to a much larger lattice mismatch of 3.06%. The CGO ($a^{CGO} = 8.328$ Å,[33] 0.16%) and MGO ($a^{MGO} = 8.280$ Å,[33] 0.73%) substrates provide intermediate values of lattice mismatch.

We examined the x-ray absorption spectroscopy (XAS) and x-ray magnetic circular dichroism (XMCD) spectra of the Fe and Ni $L_{2,3}$ core levels from NFO films grown on the four spinel substrates. These element-specific x-ray spectroscopies rely on strong dipole allowed $2p \rightarrow 3d$ electronic transitions and hence provide access to the 3*d* final states of NFO. In strongly ionic materials, XAS and XMCD are sensitive to crystal fields and can thus be used to investigate symmetry lowering around specific cations in strained films. In this study, XAS and XMCD spectra were all acquired in the total electron yield (TEY) mode. TEY is much more surface sensitive than transmission XAS/XMCD measurements, even when then transmission measurements are acquired in the substrate luminescence yield (LY) mode. XAS/XMCD acquired with TEY, therefore, provide an assessment of the 3*d* final states of NFO in the near-surface region.

II. EXPERIMENT

As mentioned, all NFO films are grown on ZGO, CGO, MGO, and MAO substrates and we refer to the resulting films as film\\substrate (e.g., NFO\\ZGO). All the substrates are spinel oxides and the films are grown using pulsed laser deposition on the [001] oriented surfaces of the spinel oxide substrates. For details on the growth of the films, please refer to Ref. 33. The deposition conditions are selected to promote epitaxial growth of the NFO films with different degrees of strain in the films, although strain relieving defects in the films increase considerably with increasing lattice mismatch between the NFO film and the spinel substrate. The thickness of the NFO films was 74 nm for the NFO\\ZGO and NFO\\MAO samples and 40 nm for NFO\\CGO and NFO\\MGO. All samples were uncapped with the exception of NFO\\CGO, where a 5 nm platinum (Pt) cap was deposited for magneto-transport measurements (not reported). A summary of the samples studied is provided in Table I.

To probe magnetic configuration and electronic states of the near-surface region of the NFO films, we utilize XAS[41,42] measured in TEY mode. XAS spectra are recorded for the L_3 ($2p_{3/2}$) and L_2 ($2p_{1/2}$) edges of Ni and Fe cations in the NFO samples. In TEY, the sample drain current is recorded as a function of the incident energy of the x-ray photons, resulting in a distribution of primary, Auger, and secondary electrons. In the soft x-ray regime, suitable for the XAS measurements of the $L_{2,3}$ edges of second row transition metals, the primary electrons have very low kinetic energy and are not capable of exciting a large number of secondary electrons. The TEY signal is dominated by very low energy secondary electrons generated by multiple inelastic scattering of Auger electrons. As these low energy electrons have a low probability of traveling to

TABLE I. Summary of samples studied.

Substrate	Lattice mismatch (%)	Film thickness (nm)	Cap ?
$ZnGa_2O_4$ (ZGO)	0.10	74	No
$CoGa_2O_4$ (CGO)	0.16	40	Yes (Pt—5 nm)
$MgGa_2O_4$ (MGO)	0.73	40	No
$MgAl_2O_4$ (MAO)	3.06	74	No

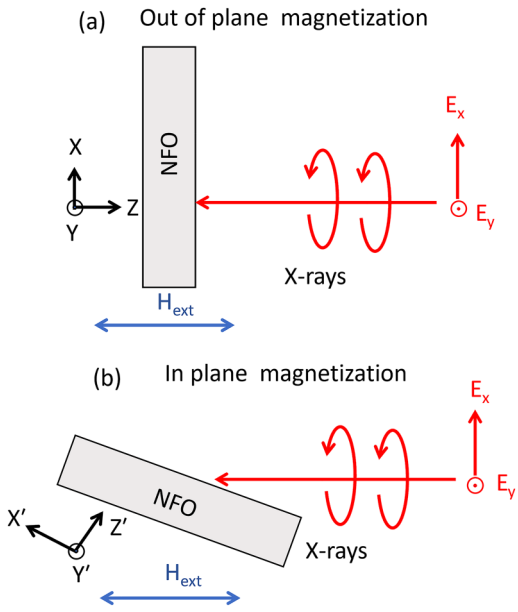

FIG. 1. Schematic of the experimental setup for (a) out-of-plane (OOP, normal incidence) and (b) in-plane (IP, 70° off-normal incidence) configuration. Circularly polarized x rays are incident upon the sample. In (a) the electric field vectors (E_x and E_y) of the x rays are parallel to the sample plane. In (b), the sample is rotated by 70° and E_y remains parallel to the sample plane but E_x will mainly have a component along the sample normal. The magnetic field (H_{ext}) of ±3 T is applied along the x-ray beam direction in both experimental geometries.

the surface and escaping the sample, the TEY mean probing depth is only a few nm from the surface of the thin film.[43]

Most of the XAS spectra in this paper were measured at the PM2-VEKMAG beamline at the BESSY-II synchrotron of the Helmholtz-Zentrum, Berlin, Germany. The measurements were performed at two different configurations (Fig. 1). For the out-of-plane (OOP) configuration, the sample was oriented with the film normal direction parallel to the photon Poynting vector and a saturating magnetic field (H_{ext}) of ± 3 T was applied in a direction parallel to the x-ray propagation direction. For the in-plane (IP) geometry, the sample was rotated by 70° while the magnetic field direction was unchanged (Fig. 1). The field was therefore predominantly in-plane. At the PM2-VEKMAG beamline, the incident soft x-ray beam had a fixed polarization of 77% RCP and XMCD[44,45] spectra were generated by recording an XAS spectra and then reversing the polarity of the magnetic field from +3 to −3 T. This experimental configuration was used for the OOP and IP TEY XAS measurements for the NFO\\ZGO, NFO\\CGO, and NFO\\MAO films. For the NFO\\MGO sample, only IP measurements in the TEY mode were recorded at beam line 4.0.2 at the Advanced Light Source, Lawrence Berkeley National Laboratory, Berkeley, CA, USA. The NFO\\MGO sample was oriented at an angle of 45° away from the x-ray Poynting vector and saturating field of ± 1 T was applied parallel to the sample surface. All spectra presented were acquired at room temperature.

III. RESULTS AND DISCUSSIONS

In Figs. 2(a) and 2(b), the Ni XAS and XMCD spectra are shown for both the in-plane (dotted lines) and out-of-plane (solid lines) configurations. The XAS spectra contain two parts. The L_3 edge ($2p_{3/2}$ level) between ≈850–857 eV is dominated by a main peak at about 852.6 eV followed by a well-defined but weaker peak at 854.3 eV. In contrast, the L_2 edge ($2p_{1/2}$) is comprised of two peaks, which we label "A" and "B," with roughly similar intensities. The Ni XAS and XMCD spectra are consistent for all the samples and also with previously published Ni-spectra for ferrites.[46–48] For NFO\\MGO, only in-plane spectra were acquired.

The Ni $L_{2,3}$ spectra are generally similar to one another. To assess small differences in the spectra, we calculate the normalized

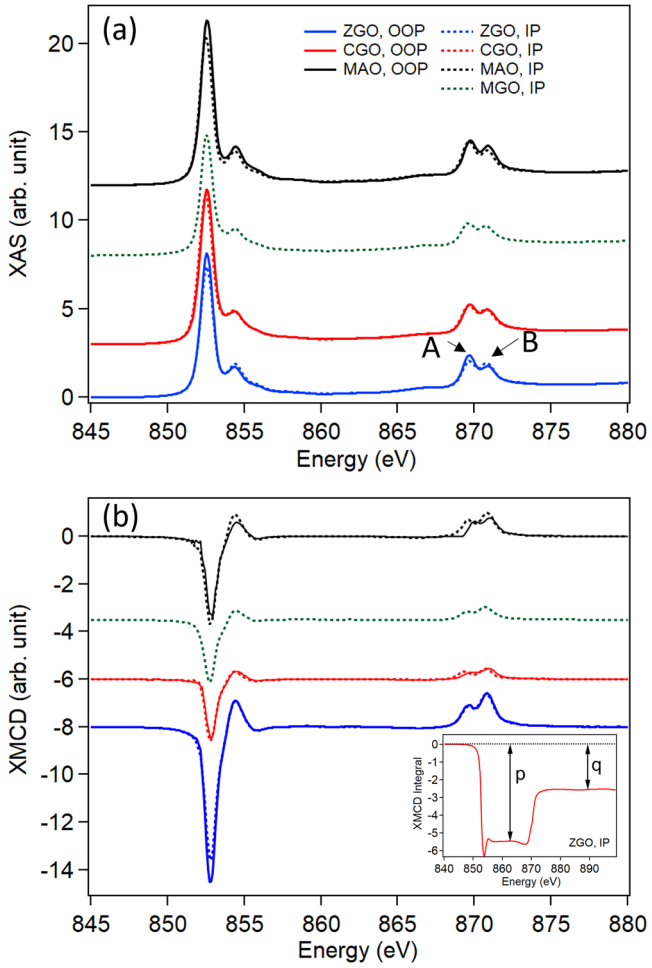

FIG. 2. (a) Polarization averaged XAS spectra of the Ni $L_{2,3}$ edges for both the IP and OOP configurations. (b) XMCD scans of the Ni $L_{2,3}$ edges. An offset in the vertical axis is added to the spectra for clarity. The IP and OOP spectra are shown by dotted and solid lines, respectively. The primary peaks at the L_2 edge are labeled by "A" and "B." The XMCD integral for the ZGO, IP sample is shown in the inset of (b).

XAS intensity difference at Ni L_3 edge, $\Delta R = (I_{OOP}\text{-}I_{IP})/I_{OOP}$ for the NFO\\ZGO and NFO\\MAO samples and we have observed that the intensity difference is around 9.0% and 9.4% for the ZGO and MAO substrates, respectively. Saturation effects originating from the variation in effective electron escape depth relative to the photon penetration depth can be amplified at high angles of incidence,[49] and such effects can lead to variations in the XAS intensity on the order of the observed variations for NFO\\ZGO and NFO\\MAO. Hence, the relative similarity of ΔR for the ZGO and MAO substrates may contain contributions from both intrinsic effects, originating from changes in the electronic structure of the $NiFe_2O_4$ films on the different substrates, and extrinsic effects originating from spectral saturation. Turning to the L_2 region of the spectra, in all cases, peak A has a larger intensity than peak B. For the case of the NFO\\MGO and NFO\\CGO films, changing from an IP to an OOP geometry produces little difference in the ratio of the A and B peaks. We note that the Pt cap on the NFO\\CGO sample may suppress variations between the IP and OOP geometries because of the saturation effects noted above. However, for the NFO\\ZGO, the A and B peaks become almost equal in intensity for the IP alignment; in other words, the intensity of peak B has increased relative to peak A.

The shape of the XMCD spectra also shows a high degree of similarity between the different samples and measurement geometries. The spectra are characterized by a dominant negative feature at the L_3 edge coinciding with the main L_3 peak in the XAS spectra; in contrast, the secondary L_3 XAS peak at 854.3 eV generates a positive feature in the XMCD spectra. At the L_2 edge, the sign of the XMCD signal is positive for both the A and B peaks for all samples and measurement conditions. However, in the dichroism spectrum, the B peak is generally higher in intensity than the A peak. In general, we conclude that the overall shape of the Ni^{2+} XMCD spectra is consistent with earlier reports for $NiFe_2O_4$,[46–48] and to a first approximation the spectra are insensitive to the lattice mismatch of the $NiFe_2O_4$ with the substrate. However, the integrated intensity distribution between the L_3 and L_2 edges displays subtle shifts, as discussed below. In the inset of Fig. 2(b), we show the integrated XMCD spectrum of ZGO, IP, where we also indicate the "p" and "q" parameters[45] which are used to calculate the orbital to spin angular momentum (μ_ℓ/μ_s) in Fig. 5.

Figures 3(a) and 3(b) present the XAS and XMCD spectra for the Fe L_3 (≈705–712 eV) and L_2 (≈719–723 eV) edge for the IP and OOP configuration. The L_3 edge is characterized by two main spectral features: a weaker peak at ∼707.3 eV and the dominant L_3 peak ∼708.8 eV. In some cases, the weaker peak at ∼707 eV appears as more of a shoulder on the main L_3 feature. In prior reports,[46] this weaker feature has been associated with a small contribution from Fe^{2+} cations which may be introduced in the sample via oxygen vacancies and other defects. As is the case with the Ni spectra, the Fe L_2 features are comprised of two primary features. Among the different samples, the Fe XAS spectra at the L_3 edge has a larger amplitude for out-of-plane configuration with respect to the in-plane one for NFO\\ZGO, NFO\\CGO, and NFO\\MAO.

For the XMCD spectrum of the Fe L_3 edge, the normalized XMCD exhibits a distinctive negative/positive/negative structure [labeled I, II, III in Fig. 3(b)], which was also previously observed

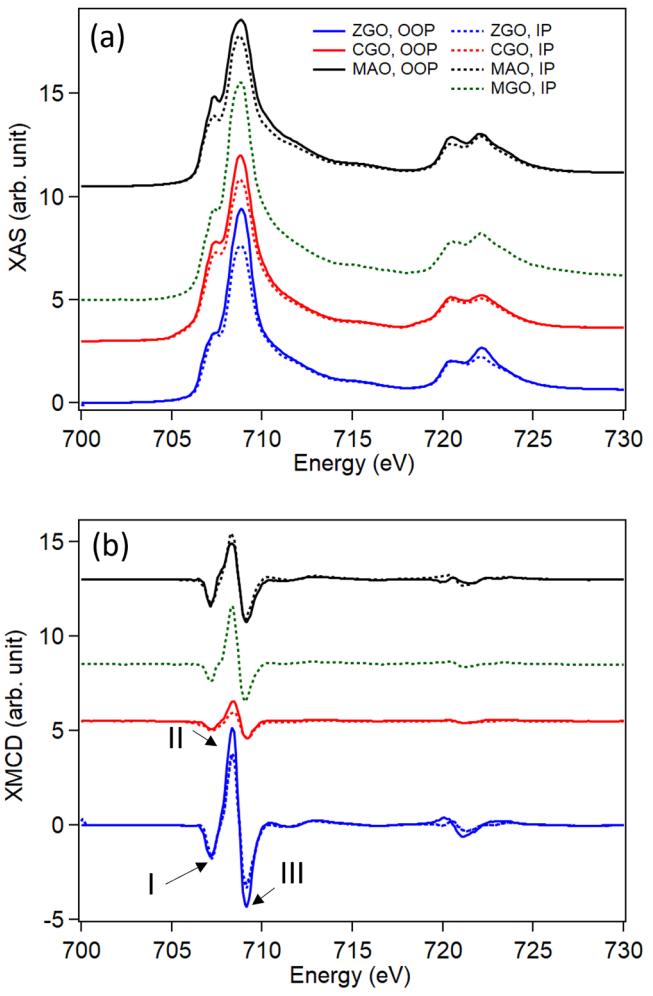

FIG. 3. (a) Polarization averaged XAS spectra of the Fe $L_{2,3}$ edges for both the IP and OOP configurations. (b) XMCD scans of the Fe $L_{2,3}$ edges. An offset in the vertical axis is added to the spectra for clarity. The IP and OOP spectra are shown by dotted and solid lines, respectively. The primary spectral features of the Fe L_3 edge are marked by "I," "II," and "III.".

for other spinel ferrites.[23,46,50] The lowest energy negative feature I is most likely a contribution from a small amount of Fe^{2+} originating from defect states.[51] XMCD spectral features II and III are associated with Fe^{3+} cations on T_d and O_h sites, respectively. The opposite signs of the two features, and the dominant negative feature on the octahedrally-coordinated Ni^{2+} XMCD spectra, confirms that cations on the O_h and T_d site are coupled antiferromagnetically. In all the XMCD spectra, the intensity of feature I is smaller compared to the intensity of both features II and III. For NFO\\ZGO, the out-of-plane intensity is larger compared to the in-plane intensity for II and III. For NFO\\MAO, the Fe XMCD features I and III have the nearly the same amplitude for both IP and OOP configuration whereas feature B has a larger

intensity for the IP spectra than the OOP one. Overall, however, the overlapping spectral features from the diverse Fe cations found in many spinel ferrites, complicates the detailed analysis of the Fe spectra.

To get a qualitative insight into the electronic states of the $NiFe_2O_4$, we model the Ni XAS spectra using the CTM4XAS (charge transfer multiplet for XAS) software package[52] for both the IP and OOP configurations. The charge transfer multiplet approach is well suited to ionic compounds such as $NiFe_2O_4$ where localized excitations of core-level electrons lead to atomic-like spectra dominated by dipole-allowed transitions between different angular momenta states which are then modified by crystal field and charge transfer effects. To generate the model Ni spectra, the atomic Slater integrals F_{dd}, F_{pd}, and G_{gd} are reduced by a factor of 0.7 for all three integrals. The spin–orbit coupling is reduced by 0.977 from atomic values for the core states and is left unchanged for the valence level final states. Lifetime and instrumental broadening effects are included by convolving the individual delta function-like multiplet spectra with Lorentzian and Gaussian distributions of 0.2 eV each. The parent symmetry of the Ni^{2+} spectra is O_h, reflecting the lattice site occupation of the Ni cations and we set the cubic crystal field ($10Dq$) parameter to 1.0 eV. For certain spectra, we simulate the effects of a tetragonal distortion of the cubic $NiFe_2O_4$ unit cell by reducing the symmetry of the calculations from O_h (cubic) to D_{4h}; this is implemented by setting the D_s and D_t parameters to non-zero values.

In Fig. 4(a), we present the Ni $L_{2,3}$ XAS spectra for the IP and OOP conditions acquired from the NFO\\ZGO sample. This sample has the lowest lattice mismatch between the $NiFe_2O_4$ film and the spinel oxide substrate. We focus on the L_2 edge and note that for the OOP configuration (black trace), the peak labeled A has a much higher intensity than peak B. For the IP condition (red trace), the intensity of peak A is reduced while peak B's intensity increases. The two spectral features are nearly equal in intensity for the IP condition. In Fig. 4(b), we present model calculations for the IP and OOP conditions. For purely cubic symmetry, a change in the ratio of peak A to peak B can only be realized by assuming extremely large and unphysical values of $10Dq$. However, by reducing the symmetry to D_{4h}, realized by setting the D_s value to 0.05 eV, a clear reduction of A/B intensity ratio is realized. We therefore conclude that there may be a small amount of tetragonal distortion in the $NiFe_2O_4$ epitaxial film even for substrates with low lattice mismatch (0.10% in the case of NFO\\ZGO).

Finally, we return to the experimental XMCD spectra for Ni and use the XMCD sum rules to calculate the ratio of the orbital to spin angular momentum (μ_ℓ/μ_s) from the integral of the XMCD spectra.[45] In Fig. 5, we present these ratios as a function of the lattice mismatch between the $NiFe_2O_4$ film and the different spinel oxide substrates. While the data set is sparse as there are not that many single crystal spinel oxide substrates available with the appropriate unit cell size, an interesting relationship is suggested by the data. For the systems with relatively low lattice mismatch (NFO\\ZGO and NFO\\CGO) there is little difference between μ_ℓ/μ_s measured in the IP or OOP configurations; no conclusions can be drawn for the NFO\\MGO sample as only IP data were collected. For the NFO\\ZGO system, which has a very low lattice mismatch of 0.10%, μ_ℓ/μ_s is about 0.15–0.16, and this ratio seems

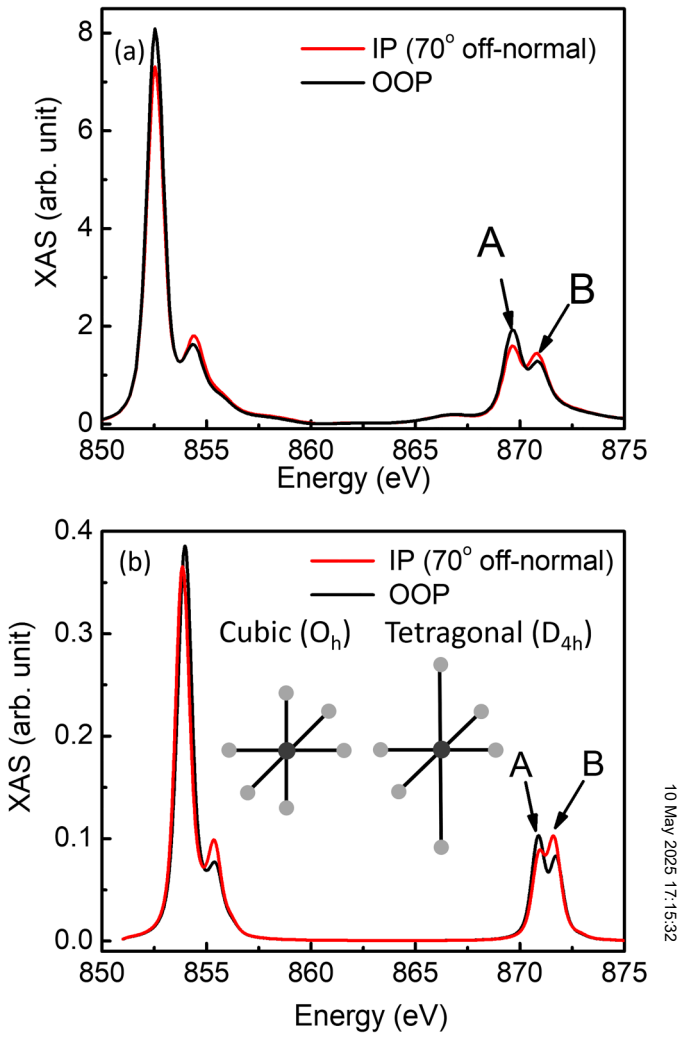

FIG. 4. (a) Experimental XAS spectra for the Ni $L_{2,3}$ edges (predominantly Ni^{2+}) for the NFO//ZGO sample. Both IP and OOP configurations are presented at $H_{ext} = 3$ T. (b) Simulated XAS spectra from a charge transfer multiplet model; crystal field parameters are 10 Dq = 1.0 eV and $D_s = 0.05$ eV. The primary peaks on the L_2 core level are marked by "A" and "B."

to grow to 0.20–0.22 for NFO\\CGO and NFO\\MGO samples with slightly higher lattice mismatch.

For the NFO\\MAO system with a large lattice mismatch of 3.06%, there is a relatively large split in μ_ℓ/μ_s for IP ($\mu_\ell/\mu_s \simeq 0.13$) and OOP (0.17). The average value between the two configurations is about 0.15 and is quite close to μ_ℓ/μ_s for NFO\\ZGO, the sample with the lowest amount of lattice mismatch. However, the NFO\\MAO film is relatively thick (74 nm) and a large number of anti-phase boundaries and other strain-relaxing defects have been reported in this sample.[33] The near-surface region of the 74 nm thick film, which is the portion of the film sampled by the XAS measured with TEY, is relaxed close to the bulk $NiFe_2O_4$ lattice

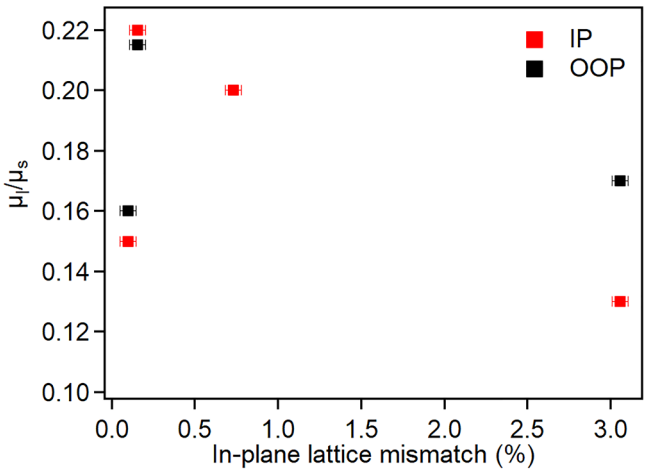

FIG. 5. Orbital to spin magnetic moment ratio (μ_ℓ/μ_s) for Ni obtained from the experiment as a function of lattice mismatch for both IP and OOP configurations. Low values of lattice mismatch, where the NFO film is coherently strained, result in an enhanced μ_ℓ/μ_s. The horizontal error bars account for differences in the reported values of the bulk NFO lattice parameter.[33,40]

parameter. In other words, the near-surface region of the NFO\\MAO film is in a strain state similar to bulk $NiFe_2O_4$. Under such conditions, the electronic states sampled by XAS in TEY mode for the NFO\\MAO and NFO\\ZGO films are similar.

IV. CONCLUSIONS

We report on the Fe and Ni $L_{2,3}$ XAS and XMCD spectra for $NiFe_2O_4$ samples grown on different substrates, namely, $ZnGa_2O_4$, $CoGa_2O_4$, $MgGa_2O_4$, and $MgAl_2O_4$. These substrates share the same spinel symmetry as the $NiFe_2O_4$ films but provide a different degree of lattice mismatch between the film and substrate. The Fe L_3 XMCD spectra exhibit a negative/positive/negative structure, similar to other spinel ferrites, and the significant amplitude of the lowest energy negative XMCD feature may indicate the presence of Fe^{2+} cations in the samples, possibly introduced by oxygen vacancies in the films. The Ni XAS spectra are generally similar across all samples and measurement geometry. The Ni L_2 edge is characterized by a two-peak structure and there is a trend of a reduction of the low energy peak (peak A) to high energy peak (B) intensity ratio when the XAS is measured at more glancing incidence (IP configuration). Our CTM4XAS modeling qualitatively reproduced this trend in the Ni L_2 edge XAS spectra and a suggests there may be a small tetragonal distortion in the system even for very low values of lattice mismatch.

Finally, we report on the Ni μ_ℓ/μ_s for the different samples and measurement conditions. While the data set is sparse, there is a trend to a larger μ_ℓ/μ_s with increasing lattice mismatch. However, this increase is not apparent in samples with large (3.06%) lattice mismatch. As the NFO\\MAO film with the large lattice mismatch was relatively thick, this suggests an intriguing possibility. The density of strain relieving defects such as misfit dislocations increases above some critical thickness and it may be feasible to stabilize highly strained films in very thin $NiFe_2O_4$ films, similar to the strategy employed to realize unusually high strain states of over 6% in perovskite on perovskite thin films.[18] This may open up a route to achieve very high orbital moments in $NiFe_2O_4$ and related compounds by growing very thin films to maintain the desired strain state. Combining such highly strained, but low defect density, films with the low damping already realized in thicker $NiFe_2O_4$ films,[33,40] may be a useful path for making further use of orbital angular momentum in spintronic and magnonic applications.

ACKNOWLEDGMENTS

S.S. gratefully acknowledges financial support of Science and Engineering Research Board, India with File No. SRG/2022/000191 and the Axis bank grant at Ashoka University, India for the funding. We also acknowledge the Swedish Research Council (2021-5395) and Carl Tryggers Foundation (17:241). This material is based upon work supported by the National Science Foundation under Grant No. ECCS-1952957. D.A.A. acknowledges support of the USF Nexus Initiative and the Swedish Fulbright Commission. We thank Cristoph Klewe for assistance with the XAS spectrum acquired at the Advanced Light Source, Berkeley, CA.

AUTHOR DECLARATIONS

Conflict of Interest

The authors have no conflicts to disclose.

Author Contributions

S. Saha: Conceptualization (equal); Data curation (equal); Formal analysis (equal); Investigation (equal); Visualization (equal); Writing – original draft (equal); Writing – review & editing (equal). **R. Knut:** Conceptualization (equal); Data curation (equal); Formal analysis (equal); Investigation (equal); Methodology (equal); Visualization (equal); Writing – original draft (equal); Writing – review & editing (equal). **A. Gupta:** Investigation (equal); Resources (equal). **F. Radu:** Data curation (supporting); Investigation (equal); Resources (supporting); Writing – review & editing (equal). **C. Luo:** Data curation (equal); Investigation (equal); Resources (equal); Writing – review & editing (equal). **O. Karis:** Conceptualization (equal); Writing – review & editing (equal). **D. A. Arena:** Conceptualization (equal); Data curation (equal); Formal analysis (equal); Funding acquisition (equal); Investigation (equal); Supervision (equal); Visualization (equal); Writing – original draft (equal); Writing – review & editing (equal).

DATA AVAILABILITY

The data that support the findings of this study are available from the corresponding author upon reasonable request.

REFERENCES

[1]S. B. Zhang and S.-H. Wei, Appl. Phys. Lett. **80**, 1376 (2002).
[2]M. Pardavi-Horvath, J. Magn. Magn. Mater. **215-216**, 171 (2000).
[3]U. Lüders *et al.*, Appl. Phys. Lett. **88**, 082505 (2006).

[4]N. M. Caffrey, D. Fritsch, T. Archer, S. Sanvito, and C. Ederer, Phys. Rev. B **87**, 024419 (2013).
[5]D. Johnston, H. Prakash, W. Zachariasen, and R. Viswanathan, Mater. Res. Bull. **8**, 777 (1973).
[6]P. K. Baltzer, H. W. Lehmann, and M. Robbins, Phys. Rev. Lett. **15**, 493 (1965).
[7]A. Yanase and K. Siratori, J. Phys. Soc. Jpn. **53**, 312 (1984).
[8]Y. Ogimoto, M. Nakamura, N. Takubo, H. Tamaru, M. Izumi, and K. Miyano, Phys. Rev. B **71**, 060403 (2005).
[9]I. Bozovic, G. Logvenov, I. Belca, B. Narimbetov, and I. Sveklo, Phys. Rev. Lett. **89**, 107001 (2002).
[10]F. M. D. Pellegrino, G. G. N. Angilella, and R. Pucci, Phys. Rev. B **81**, 035411 (2010).
[11]B. Conings, L. Baeten, C. De Dobbelaere, J. D'Haen, J. Manca, and H.-G. Boyen, Adv. Mater. **26**, 2041 (2014).
[12]D. Çakır, H. Sahin, and F. M. C. M. Peeters, Phys. Rev. B **90**, 205421 (2014).
[13]T. J. Pennycook, M. J. Beck, K. Varga, M. Varela, S. J. Pennycook, and S. T. Pantelides, Phys. Rev. Lett. **104**, 115901 (2010).
[14]T. Guan *et al.*, Phys. Rev. Lett. **115**, 087002 (2015).
[15]E. Paz, R. Ferreira, and P. P. Freitas, IEEE Trans. Magn. **52**, 1 (2016).
[16]R. Nirmala *et al.*, J. Phys.: Condens. Matter **29**, 13LT01 (2017).
[17]A. V. Zakrzewski, S. Gangopadhyay, G. J. MacDougall, A. A. Aczel, S. Calder, and T. J. Williams, Phys. Rev. B **97**, 214411 (2018).
[18]D. G. Schlom, L.-Q. Chen, C. J. Fennie, V. Gopalan, D. A. Muller, X. Pan, R. Ramesh, and R. Uecker, MRS Bull. **39**, 118 (2014).
[19]X. J. Chen, S. Soltan, H. Zhang, and H. U. Habermeier, Phys. Rev. B Condens. Matter Mater. Phys. **65**, 1744021 (2002).
[20]D. Meng *et al.*, Proc. Natl. Acad. Sci. U.S.A. **115**, 2873 (2018).
[21]S. F. Rus, T. Z. Ward, and A. Herklotz, Thin Solid Films **615**, 103 (2016).
[22]B. Yildiz, MRS Bull. **39**, 147 (2014).
[23]J.-S. Kang *et al.*, Phys. Rev. B **77**, 035121 (2008).
[24]C. L. Chen *et al.*, Supercond. Sci. Technol. **24**, 115007 (2011).
[25]T. Omata, N. Ueda, K. Ueda, and H. Kawazoe, Appl. Phys. Lett. **64**, 1077 (1994).
[26]Z. Szotek, W. M. Temmerman, D. Ködderitzsch, A. Svane, L. Petit, and H. Winter, Phys. Rev. B **74**, 174431 (2006).
[27]J. Smith and H. P. J. Wijn, *Ferrites: Physical Properties of Ferrimagnetic Oxides in Relation to Their Technical Applications* (Philips Technical Library, Eindhoven-Holland, 1965).
[28]U. Lueders, M. Bibes, J. F. Bobo, M. Cantoni, R. Bertacco, and J. Fontcuberta, Phys. Rev. B **71**, 134419 (2005).
[29]Q. C. Sun *et al.*, Phys. Rev. B **86**, 205106 (2012).
[30]G. H. Jaffari, A. K. Rumaiz, J. C. Woicik, and S. I. Shah, J. Appl. Phys. **111**, 93906 (2012).
[31]K. Kamala Bharathi, K. Balamurugan, P. N. Santhosh, M. Pattabiraman, and G. Markandeyulu, Phys. Rev. B Condens. Matter Mater. Phys. **77**, 172401 (2008).
[32]R. H. Kodama, A. E. Berkowitz, E. J. McNiff Jr., and S. Foner, Phys. Rev. Lett. **77**, 394 (1996).
[33]A. V. Singh *et al.*, Adv. Mater. **29**, 1701222 (2017).
[34]U. Lüders *et al.*, Adv. Mater. **18**, 1733 (2006).
[35]G. H. Jaffari, A. K. Rumaiz, J. C. Woicik, and S. I. Shah, J. Appl. Phys. **111**, 093906 (2012).
[36]A. Khorshidi, J. Violet, J. Hashemi, and A. A. Peterson, Nat. Catal. **1**, 263 (2018).
[37]S. Zhang, X. Zhang, G. Jiang, H. Zhu, S. Guo, D. Su, G. Lu, and S. Sun, J. Am. Chem. Soc. **136**, 7734 (2014).
[38]D. Fritsch and C. Ederer, Phys. Rev. B **82**, 104117 (2010).
[39]R. Datta, S. Kanuri, S. V. Karthik, D. Mazumdar, J. X. Ma, and A. Gupta, Appl. Phys. Lett. **97**, 071907 (2010).
[40]S. Regmi *et al.*, Appl. Phys. Lett. **118**, 152402 (2021).
[41]G. van der Laan and I. W. Kirkman, J. Phys.: Condens. Matter **4**, 4189 (1992).
[42]S. C. Wi *et al.*, Appl. Phys. Lett. **84**, 4233 (2004).
[43]B. H. Frazer, B. Gilbert, B. R. Sonderegger, and G. De Stasio, Surf. Sci. **537**, 161 (2003).
[44]B. T. Thole, P. Carra, F. Sette, and G. van der Laan, Phys. Rev. Lett. **68**, 1943 (1992).
[45]C. T. Chen, Y. U. Idzerda, H.-J. Lin, N. V. Smith, G. Meigs, E. Chaban, G. H. Ho, E. Pellegrin, and F. Sette, Phys. Rev. Lett. **75**, 152 (1995).
[46]R. Knut *et al.*, J. Phys.: Condens. Matter **33**, 225801 (2021).
[47]C. Klewe, M. Meinert, A. Boehnke, K. Kuepper, E. Arenholz, A. Gupta, J.-M. Schmalhorst, T. Kuschel, and G. Reiss, J. Appl. Phys. **115**, 123903 (2014).
[48]G. van der Laan, C. M. B. Henderson, R. A. D. Pattrick, S. S. Dhesi, P. F. Schofield, E. Dudzik, and D. J. Vaughan, Phys. Rev. B **59**, 4314 (1999).
[49]R. Nakajima, J. Stöhr, and Y. U. Idzerda, Phys. Rev. B **59**, 6421 (1999).
[50]J. A. Moyer, C. A. F. Vaz, D. A. Arena, D. Kumah, E. Negusse, and V. E. Henrich, Phys. Rev. B **84**, 054447 (2011).
[51]C. Kons, M.-H. Phan, H. Srikanth, D. A. Arena, Z. Nemati, J. A. Borchers, and K. L. Krycka, Phys. Rev. Mater. **4**, 034408 (2020).
[52]E. Stavitski and F. M. de Groot, Micron **41**, 687 (2010).